ABSTRACT

Title of Thesis: MEASUREMENT OF INVERSE DIFFUSION FLAME QUENCHING LIMITS

Yi Zhang, Master of Science, 2013

Directed By: Associate Professor Peter B. Sunderland
Department of Fire Protection Engineering

Quenching limits of inverse diffusion flames were measured for different conditions. The flames were laminar and axisymmetric and were obtained by injecting various oxidizers into fuels. Burner inside diameters were 0.75, 1.53, 3.02, 4.56, and 10.1 mm. Oxygen mole fractions were 0.21, 0.3, 0.4, and 1, and the balance was nitrogen. Fuels were methane, ethylene, and propane. The flames were observed in a weak co-flow of fuel inside a glass chimney. The flames were ignited at relatively high oxidizer flow rates, after which the oxidizer flow was reduced until extinction. The typical heat release rate of quenching inverse flame ranged from 1 – 2 W, compared to a typical heat release rate of quenching normal hydrocarbon flames of 3 W. The quenching limits of inverse flames were generally independent of burner diameter, were proportional to the fuel quenching distance in premixed flames, and scaled with $X_{O2}^{-1.5}$. The results may help assess the hazards of firefighter respirator leaks in underventilated fires.

MEASUREMENT OF INVERSE DIFFUSION FLAME QUENCHING LIMITS

By

Yi Zhang

Thesis submitted to the Faculty of the Graduate School of the
University of Maryland, College Park, in partial fulfillment
of the requirements for the degree of
Master of Science
2013

Advisory Committee:
Associate Professor Peter B. Sunderland, Chair
Professor Emeritus James G. Quintiere
Assistant Professor Stanislav I. Stoliarov

Acknowledgements

This work is supported by NIOSH. Without the funding, the work might not be possible on the first place and I would not have the chance to get involved in this meaningful work that might provide some useful information in the firefighter safety applications.

I would like to thank all the people in the fire protection department. It is their warming kindness and helpfulness that make this comfortable environment for the daily learning and working. The friendship I found here help me relief the loneliness of being away from my family and hometown. The teachers lectured me with great patience and encouragement. Most of all, I would like to recognize my advisors, Dr. Sunderland and Dr. Quintiere. Dr. Sunderland gave me great help and faith without any hesitation when I, as a new foreign student, talked to him at his office for the first time. In the progress of this project, he kindly offered invaluable suggestions and guidance. Although Dr. Quintiere didn't get involved directly in this project, I learned a lot and gained inspiration from his passion and attitude toward his work and life. I am very fortunate to have the chance working with these knowledgeable and nice people.

Last but not least, I would like to thank my parents. They are very supportive to my study overseas even though they miss me so hard. No matter how difficult the situation I am facing, I know they are always on my back. There is just not enough gratitude to them I could express.

Contents

Acknowledgements ii

List of Figures iv

List of Tables vi

List of Symbols vii

1. Introduction 1

1.1 Background 1

1.2 Correlations 4

1.3 Objectives 5

2. Literature Review 6

2.1 Oxygen leak from the firefighter mask 6

2.2 Inverse flame 8

2.3 Quenching limit 18

3. Experimental 28

4. Results 33

5. Conclusions 40

References 41

List of Figures

Figure 1.1 A demonstration of a methane inverse flame [3] 4
Figure 2.1 Time sequence of velocity vectors [2] 7
Figure 2.2 Top view of the oxygen leakage from the respirator [2] 7
Figure 2.3 Flammability diagram of Propane [2] 8
Figure 2.4 Comparison of inverse Jet flame with increased oxygen concentration in 1g and microgravity [4] 9
Figure 2.5 Schematic of a co-flow burner [5] 10
Figure 2.6 Experimental and predicted flame height results depending on the air flow rate [5] 11
Figure 2.7 Peak PAH, OH and soot PLII contours in the ethylene (top) and methane (bottom) inverse flame. [13] 12
Figure 2.8 Schematic of the natural gas inverse flame burner [6] 14
Figure 2.9 The sequence of the natural gas inverse flames with increased air flow. [6] 14
Figure 2.10 Shaddix's experimental set up for the inverse flame [15] 16
Figure 2.11 Color images of microgravity flames from the burner. (a) Ethylene issuing into air (b) diluted ethylene issuing into oxygen (c) air issuing into ethylene (d) oxygen issuing into diluted ethylene. [16] 17
Figure 2.12 Methane flames close to the quenching limits. [8] 19
Figure 2.13 Methane quenching velocity as a function of tube diameter [8] 20
Figure 2.14 Computed OH mass fraction contour near the extinction limit [8] 21
Figure 2.15 Mass flow rates at quenching and blow off limits with respect to tube diameter [10] 22
Figure 2.16 Different configurations of the round-hole burner [10] 23
Figure 2.17 The quenching mass flow rates of different burner configurations [10] 23
Figure 2.18 The quenching mass flow rates of different burner orientations [10] 24
Figure 2.19 Propane flames close to the quenching limits [7] 25
Figure 2.20 Quenching limit as a function of ambient temperature [7] 25

Figure 2.21 Equivalence ratio near quenching and blow-off with respect to radius [7] 26
Figure 2.22 Numerical simulation of the flame close to the quenching limit [8].....27
Figure 3.1 Schematic for the burner 28
Figure 3.2 Pressure vessel.....29
Figure 3.3 Flow system.....30
Figure 3.4 Colored photo of the experimental set up with the inverse flame at the center.....31
Figure 3.5 Calibration of the rotameter measurements.....31
Figure 4.1 Color images of inverse flames close to their quenching limits.....33
Figure 4.2 Color photos of the flame near quenching limits for all the tests.....34
Figure 4.3 Quenching mass flow rate of oxidizers injecting into CH_4, C_2H_4 and C_3H_8 with respect to X_{O2}.....35
Figure 4.4 Quenching mass flow rate of oxidizers with respect to burner diameters..36
Figure 4.5 Quenching mass flow rate of oxidizers with respect to quenching distances 37
Figure 4.6 Heat release rate at the quenching limit with respect to burner diameter...38

List of Tables

Table 1 Differences in sooting characteristics between normal and inverse diffusion flames [18] 18

Table 2 Selected properties of methane, ethylene and propane 38

Table 3 Quenching limit measurements for all tests 39

List of Symbols

a	fuel specific constant
d	burner inner diameter
c	normalized half-width of the inner *wall*
D_0	diffusion coefficient
HRR	heat release rate
L_f	laminar diffusion flame length
L_q	premixed flame quenching distance
LFL	lower flammability limit
m_{fuel}	fuel mass flow rate
Pe	Peclet number
Q	volumetric flow rate
r	fuel-to-oxygen stoichiometric mass fraction
Re	Reynolds number
S	fuel-to-air stoichiometric volume ration
S_L	laminar burning velocity
T_0	fuel stream temperature
T_f	mean flame temperature
UFL	upper flammability limit
X	mole fraction
Y	mass fraction
Z_f^*	normalized flame height
α_n	$(Pe^2+4\pi^2n^2)^{1/2}$
Δh_c	heat of combustion
μ	dynamic viscosity

Subscripts

f	flame
F	fuel
O	oxidizer
$O2$	oxygen
q	at quenching limit

1. Introduction

1.1 Background

A self-contained breathing apparatus, or SCBA, that recycle exhaled air must remove carbon dioxide, but save oxygen and inert gases (nitrogen). Augmenting the portion of oxygen in the compressed gas cylinder would allow either extended service times with the same size cylinder or lighter weight with a smaller cylinder. It has been found that by breathing oxygen-enriched air (e.g., 40% oxygen by volume in nitrogen), firefighters can improve their physical performance and increase the operational time available from an SCBA [1]. However, many SCBA are used in firefighting or other combustible atmospheres. Oxygen-rich air mixtures leaking from the positive-pressure facepiece could pose a burn hazard for the wearer during these situations. Thus, oxygen enrichment is presently prohibited.

NIOSH has imposed a long-standing advisement against the use of oxygen-based closed-circuit respirators in the presence of high radiant heat or open flames based upon concerns of user burn injury from the potential oxygen enriched atmospheres in the vicinity of face piece leaks. Flame engulfment testing has been conducted with mixed results on closed-circuit respirators at the ETL Laboratories in Cortland, New York according to NFPA 1981 standard for open-circuit respirators. It has been revealed in these tests that the face piece fit represents the biggest problem for a closed-circuit respirator to provide adequate protection against oxygen leaks.

A typical closed-circuit respirator provides the user with three stages of oxygen supply into the breathing loop. There is: 1) a constant flow rate of air designed to accommodate a moderate rate of consumption, 2) a pressure demand flow designed to supplement oxygen supplies to users consuming oxygen above the constant rate, and 3) an emergency flow rate, designed to compensate for pressure regulator failure. The constant oxygen flow rate is usually within a range 1.5 to 2.0 Lpm while pressure demand and emergency flows are in the range of 80 to 100 Lpm. Typical steady-state maximum oxygen consumptions for people are about 3.5 Lpm or 5.5 Lpm for highly-trained individuals.

There are only two situations that cause actuation of the pressure demand oxygen flow. When a user consumes oxygen at a rate higher than the constant add, the pressure demand supplements the oxygen feed with short duration 80-100 Lpm additions. Or, should a closed-circuit respirator develop a leak in any portion of the breathing loop, escaping oxygen decreases the amount of the constant add available to the user, and will initiate pressure demand additions.

A computational fluid dynamics (CFD) simulation of oxygen leaks from the face piece of an SCBA [2] has shown that, no matter how small the leak, there is for each leak a region in which the ratio of oxygen to combustible gas is able to support combustion. It would seem, then, that any leak at all could be dangerous. However, it is not practically possible to detect oxygen leaks of the smallest magnitude. Realistic sensitivity specifications for an oxygen leak detector should be derived from information about the threat of combustion from different sized leaks.

If the seal between the respirator and face is imperfect, supplied oxygen can leak. An oxidizer leak into a hot, rich environment can result in an inverse flame, in this case one that could burn the firefighter's face and damage his or her respirator. It is not known how large of a leak would be required to present this type of hazard.

Unlike normal flames, where the fuel is surrounded by oxidizer, inverse flames are those where oxidizer is surrounded by fuel. Alan [3] presented a demonstration of air in methane inverse flame. The apparatus in their experiment, as shown in Figure 1.1, is similar to what we have in this study. A glass vessel was filled with methane and the flame was ignited on top of the vessel. Then the inner tube flowed with air was lifted from the bottom of the vessel and the inverse flame was ignited by the normal flame at the top.

Past work revealed some of the characteristics for inverse diffusion flames [4-6]. Quenching limits of normal flames have been reported by many studies [7-9]. However no investigation to date has measured the quenching limits of inverse flames.

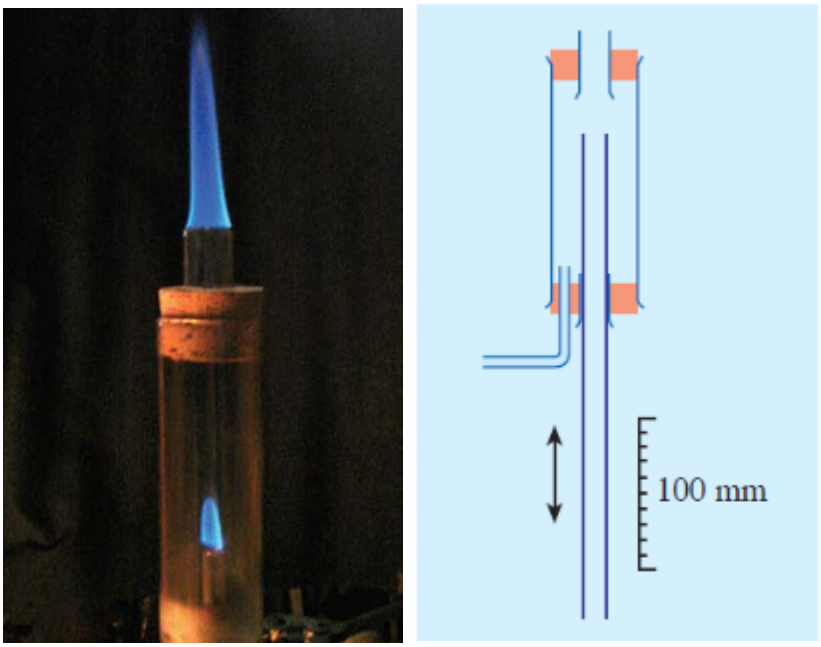

Figure 1.1 A demonstration of a methane inverse flame [3]

1.2 Correlations

A scaling analysis for quenching limit in Butler's paper [10] is presented here. Although the prediction may not work the same way for the inverse flame, it provides some guidelines to understand the result of this study. For the round-hole burners, the stoichiometric length of the laminar gas jet diffusion flames could be expressed as:

$$L_f / d = a\,\mathrm{Re} = 4m_{fuel}a / (\pi\mu d) \qquad (1.1)$$

where d is the burner inner diameter, Re is the Reynolds number, a is a fuel specific coefficient, m_{fuel} is the fuel mass flow rate and μ is the dynamic viscosity. The standoff distance of a diffusion flame could be approximated as 50 % of the quenching distance of a premixed flame. The flame would be quenched if its stoichiometric length is less than the premixed quenching distance, $L_f < L_q / 2$. Inserting this criterion back to equation (1.1) yields the following correlation

$$m_{fuel} = \pi L_q \mu / (8a) \tag{1.2}$$

Based on this correlation, the mass fuel flow rate at the quenching point is independent of the fuel port diameter.

1.3 Objectives

It is proposed here to experimentally characterize the quenching limits of inverse flames with application to firefighter safety. Quartz chimneys will surround the co-flowing fuel to prevent the formation of secondary flames. Flames will be ignited at relatively high oxidizer flow rates and then the oxidizer flow will be reduced to the point of extinction.

The fuels to be considered will be methane, propane, and ethylene. The oxidizers will be O_2/N_2 mixtures with oxygen mole fractions of 0.21, 0.3, 0.4, and 1. Co-flow burners will be used. These burners are brass with ceramic honeycomb and have central (oxidizer) ports of 1, 3, and 14 mm and concentric (fuel) ports of 100 mm.

2. Literature Review

2.1 Oxygen leak from the firefighter mask

Butler [2] used CFD to model the oxygen leak from a fire fighter masker under different scenarios and examined how it would influence the gas flammability around the wearer. The cases that were studied in this report consisted of three different surrounding fuel concentration, two different oxygen concentrations and two different breathing patterns.

Figure 2.1 shows the sequence of simulated velocity vector in the case of pure oxygen leak into pure propane. The exhalation during 1-2 s and 5-6 s induced a flow at the rate of about 1 m/s. However the flow region is very narrow and in a short distance away from that region, the flow rate reduced to about 0.2 m/s.

Figure 2.2 depicts the propane concentration near the leak. The red contour is the UFL and the LFL is very close to the leak. So anywhere between the contour and the leak is the flammable region.

Figure 2.3 is the flammability diagram of propane. For the pure oxygen, all the possible mixtures lie on the side marked by the yellow line, where the lower left corner indicates the pure oxygen and top indicates pure propane. As shown in the diagram, the LFL for the propane oxygen mixture is 2.1% and UFL is 58%.

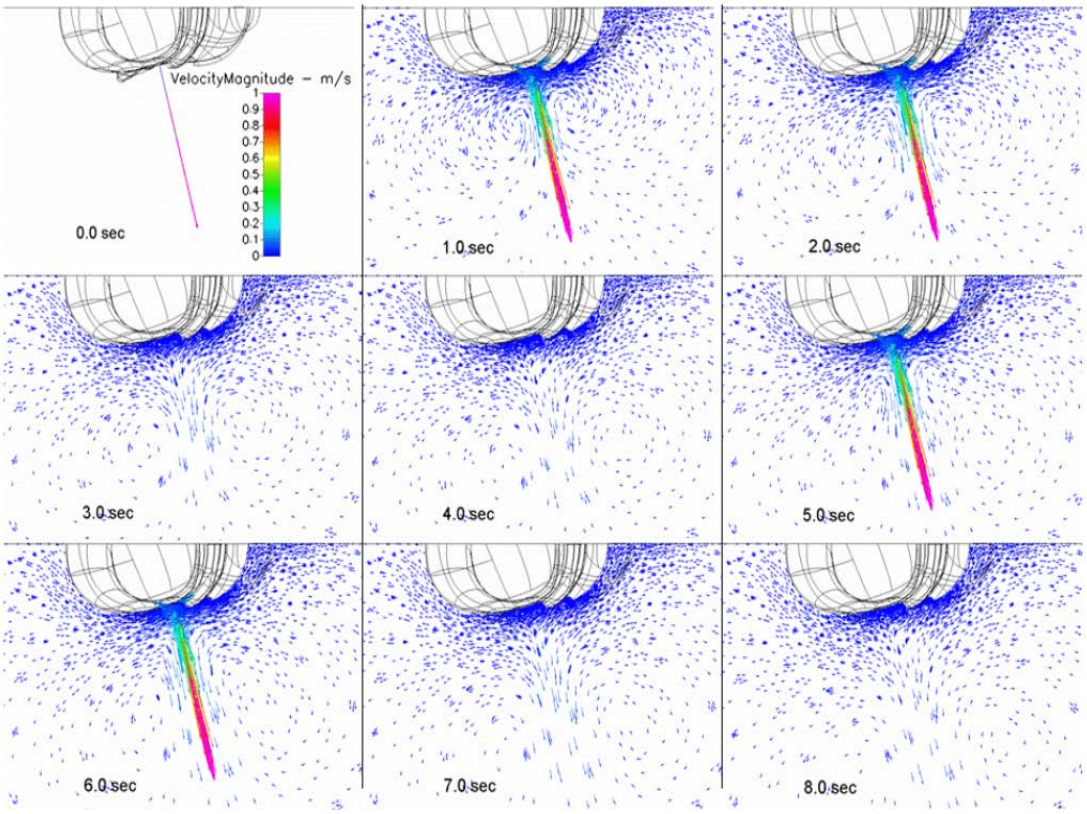

Figure 2.1 Time sequence of velocity vectors [2]

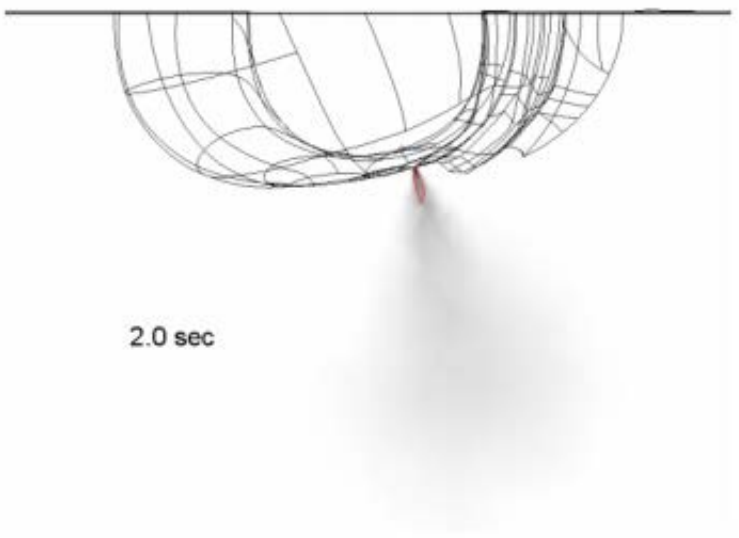

Figure 2.2 Top view of the oxygen leakage from the respirator [2]

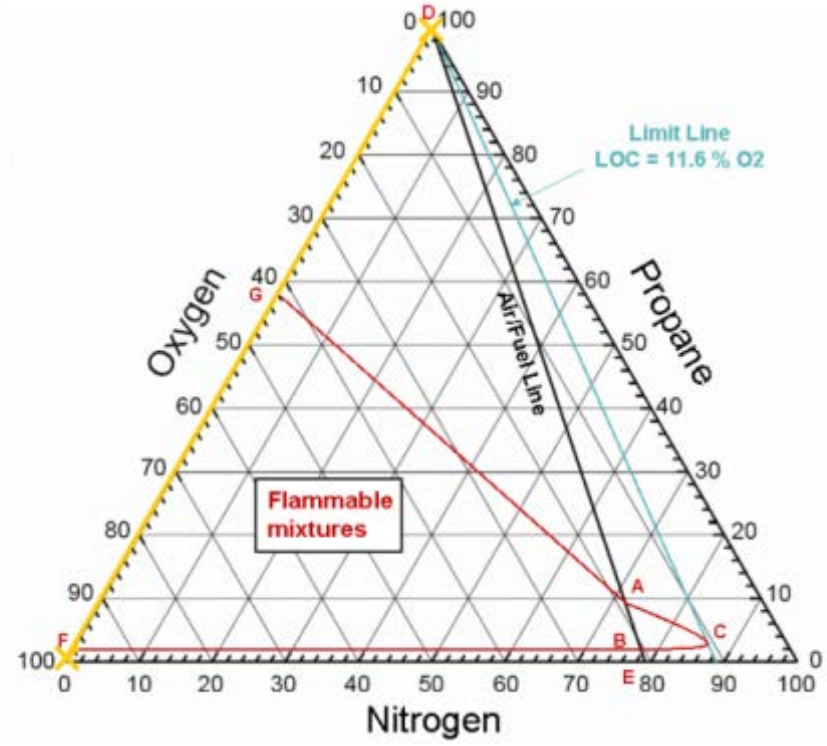

Figure 2.3 Flammability diagram of Propane [2]

In summary, the worst situation is the leakage into a fuel-rich environment. In that case, a low flow rate leakage may lead to flammability. An enhanced breathing rate under stress would enlarge the flammable region. In the scenario of pure oxygen leaking into pure fuel, the flammable region is very small and a non-flammable region is created near the leak.

2.2 Inverse flame

In 1997, there was a fire accident on Mir space station [11]. The oxygen leaked from lithium-perchlorate oxygen generator and induced an inverse flame that threatened the lives of six crew members. When a crew member initiated the oxygen generator in a canister to increase the oxygen concentration, the canister ruptured and

emitted a 0.5 m flame torch. The reactants were the oxygen jet and the fiber glass and iron in the canister case.

Motivated by the fire safety concerns in microgravity, Sunderland et al. [4] investigated the inverse flame in ethane with enhanced oxygen concentration. The oxygen concentrations were 21%, 30%, 50% and 100%. The tests were conducted in normal gravity and microgravity environment. The burner was a 5.5 mm stainless tube. The ambient gas was sealed in a 27 L cylindrical pressure vessel.

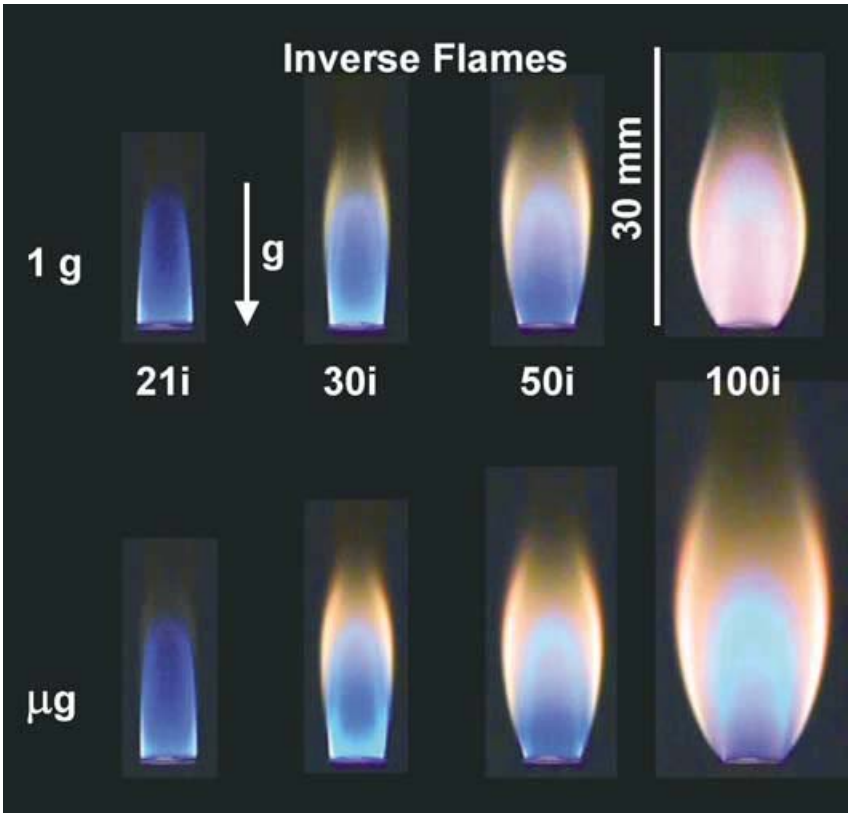

Figure 2.4 Comparison of inverse Jet flame with increased oxygen concentration in 1g and microgravity [4]

Figure 2.4 shows the results for both normal and microgravity inverse flames. They found that by enhancing the oxygen concentration, the soot production, soot emission and luminosity have been increased. The soot was formed in the fuel side of the flame.

Gravity variation had little effect on the flame shape because the convection was much more significant.

Mikofski et al. [5] measured the flame height of air-methane and air-ethylene inverse flame for different air velocities. The apparatus they used to generate an inverse flame was a co-flow burner with three concentric tubes, as shown in Figure 2.5. The air flowed through the central tube. The fuel flowed through an annulus surrounding the central tube. Nitrogen was flowed through the second annulus to prevent the secondary flame formed between the fuel and air in the ambient.

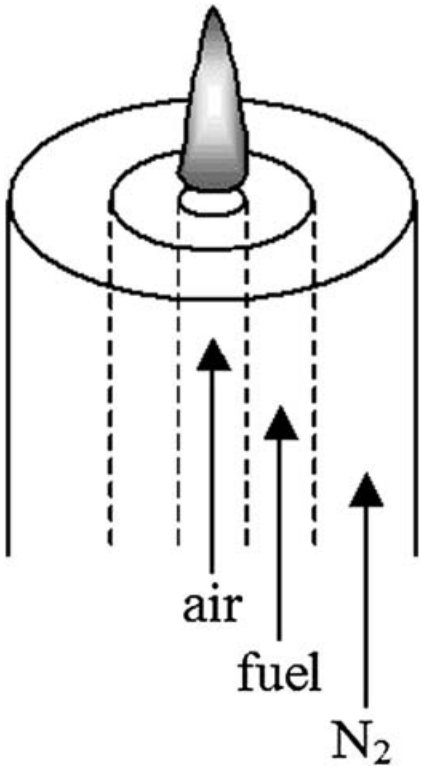

Figure 2.5 Schematic of a co-flow burner [5]

The Roper's equation [12] for the normal diffusion flame height of the circular port burner is expressed as

$$H / Q = [4\pi D_0 \ln(1+1/S)]^{-1}(T_0 / T_f)^{0.67} \quad (2.1)$$

In order to apply it for the inverse flame, the following parameters were modified:

Q is the oxidizer volumetric flow rate rather than the fuel.

S is the stoichiometric fuel-to-air volume ratio rather than air-to-fuel.

Using the modified equation, the author predicted the inverse flame height of various air flow rate and thus verified the similarity between the flame structure of normal diffusion flame and inverse diffusion flame. Figure 2.6 shows the prediction results with different flame height coefficients as well as the experimental measurements.

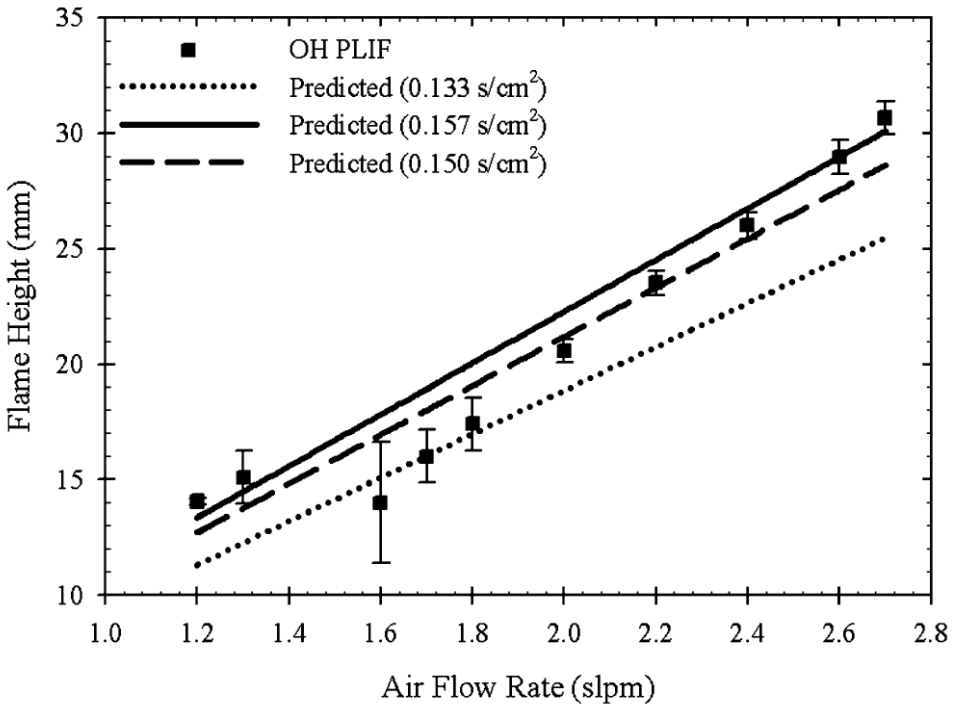

Figure 2.6 Experimental and predicted flame height results depending on the air flow rate [5]

The same co-annular burner was used to study the sooting structure in the air-ethylene inverse flame and air-methane inverse flame [13]. Planar laser-induced fluorescence of hydroxyl radicals (OH PLIF) and polycyclic aromatic hydrocarbons

(PAH PLIF), planar laser-induced incandescence of soot (soot PLII), and thermocouple determined gas temperatures were the diagnosis applied in the study. PAH is the soot precursor and OH radicals is the indication of the reaction zone.

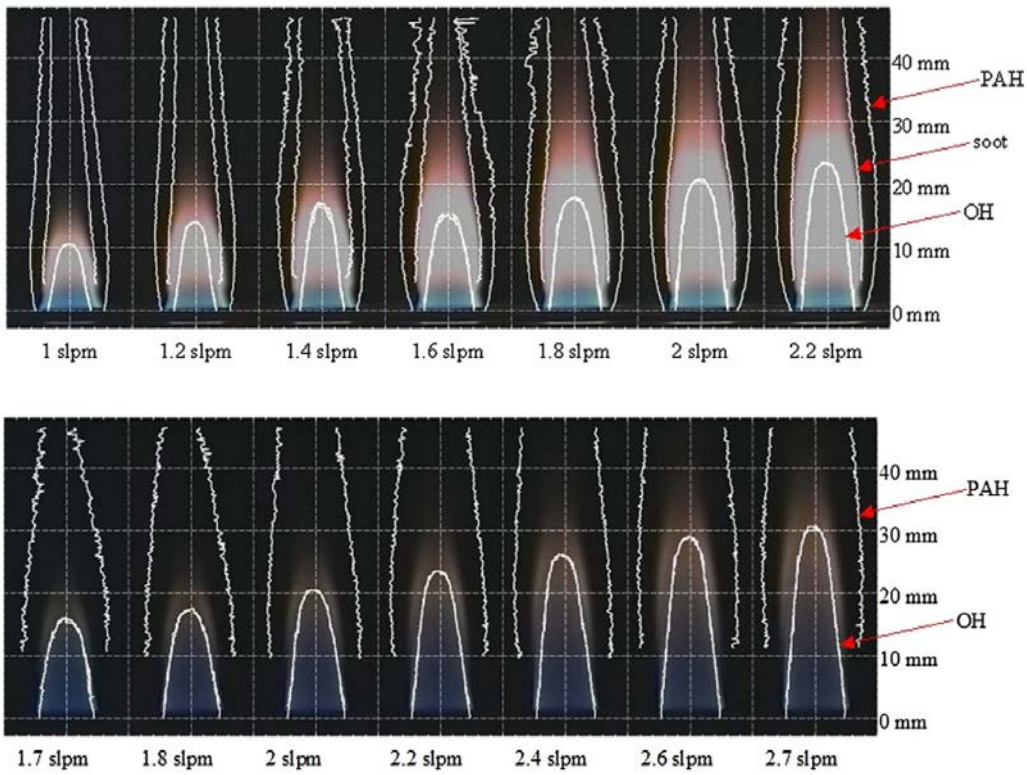

Figure 2.7 Peak PAH, OH and soot PLII contours in the ethylene (top) and methane (bottom) inverse flame. [13]

Figure 2.7 depicts the contours of the peak PAH, OH and soot PLII in the ethylene and methane inverse flame. A series of flow rates were tested to examine its effect on the flame sooting structure. The OH layer initiated at the burner is about 2mm in thickness which was similar to that for a normal diffusion flame. The PAH originated at the fuel side of the top of the burner. The radial distance of PAH and soot contour from the central axis increased at the flame region while decreased about the flame. As the air flow rate increased, the PAH signals moved further away from the central axis.

Although the soot PLII signal was not detect in the methane flame, a luminous smoke layer could be seen from the color photo.

Sobiesiak et al. [6] studied the characteristics of natural gas inverse flames using a similar co-flow burner. The schematic of this burner is depicted in Figure 2.8. The burner had three annular tubes, which delivered air, natural gas and nitrogen. A honeycomb section was placed in the nitrogen tube to ensure a uniform flux. They changed the fuel to air tube diameter ratio and measured the temperature and flame length. Figure 2.9 shows the sequence of increasing the air flow at the central tube. Initially a normal diffusion flame was established without the air flow in Figure 2.9A. Then the air flow was gradually increased through the sequence form B to D. A light blue flame structure was created inside the normal flame. Then the normal diffusion flame was opened at the tip and leaded to a flame blow-out. In Figure 2.9D, only the inner inverse flame remained.

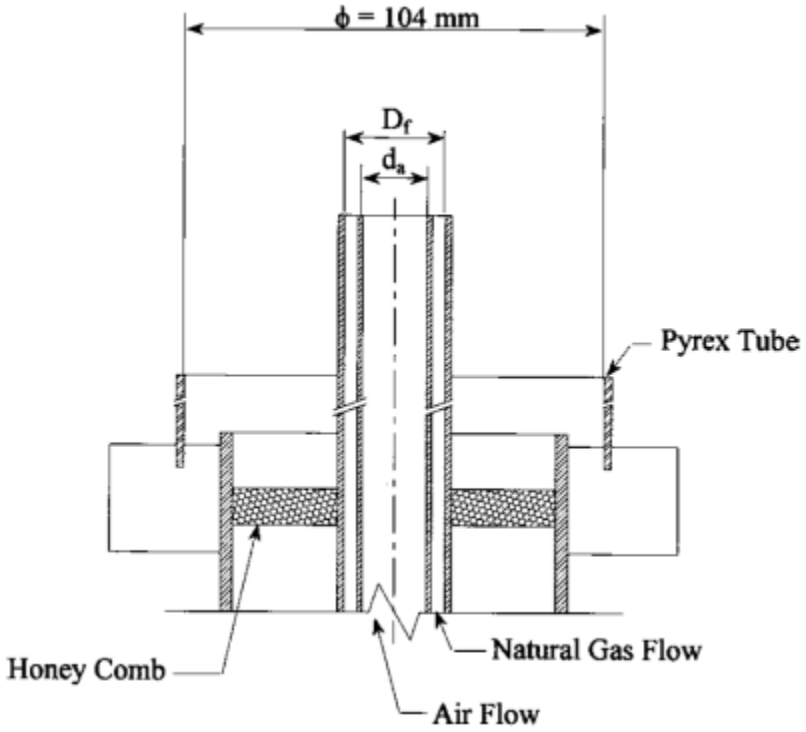

Figure 2.8 Schematic of the natural gas inverse flame burner [6]

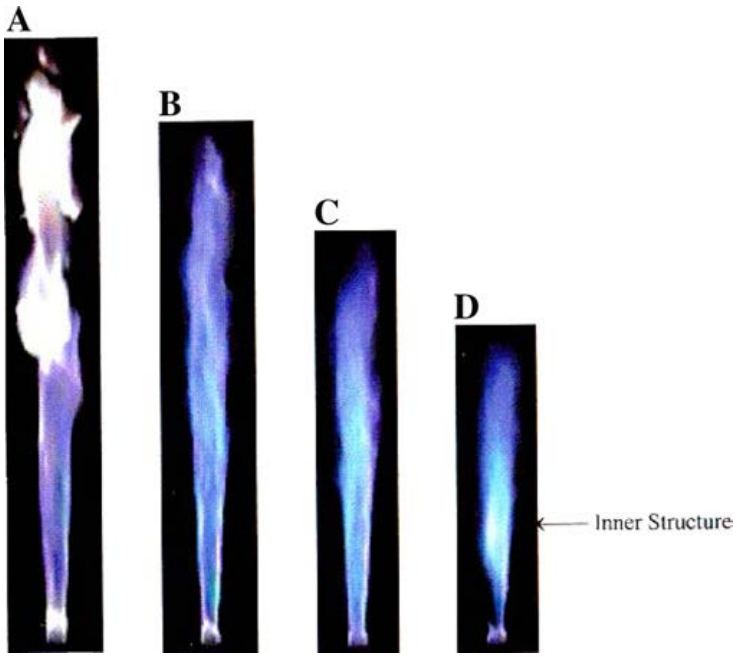

Figure 2.9 The sequence of the natural gas inverse flames with increased air flow. [6]

Shaddix et al.[14] studied steady and pulsed inverse flames set up on a slot burner as shown in Figure 2.10. OH and PAH laser induced fluorescence (LIF), soot laser-induced incandescence (LII), and soot thermal emission have been measured in the lower flame region to study the flame structure and soot formation.

Soot is formed in the fuel side of a diffusion flame. In the case of an inverse diffusion flame, soot is formed outside of the flame sheet at the downstream of the convection. Thus it does not experience the high temperature flame sheet and leaves the flame unoxidized. Soot collected from the inverse flame is tarlike and has high hydrogen content. As far as the chemical composition, they are close to those collected from the underventilated normal diffusion flames.

Blevins et al. [15] found that inverse flames facilitated the collection of soot precursors and early soot. They propose the hypothesis that the early soot precursors could be collected in the exhausts of the inverse diffusion flame and validate it by post analysis of the soot. Their experimental set up is shown in Figure 2.10.

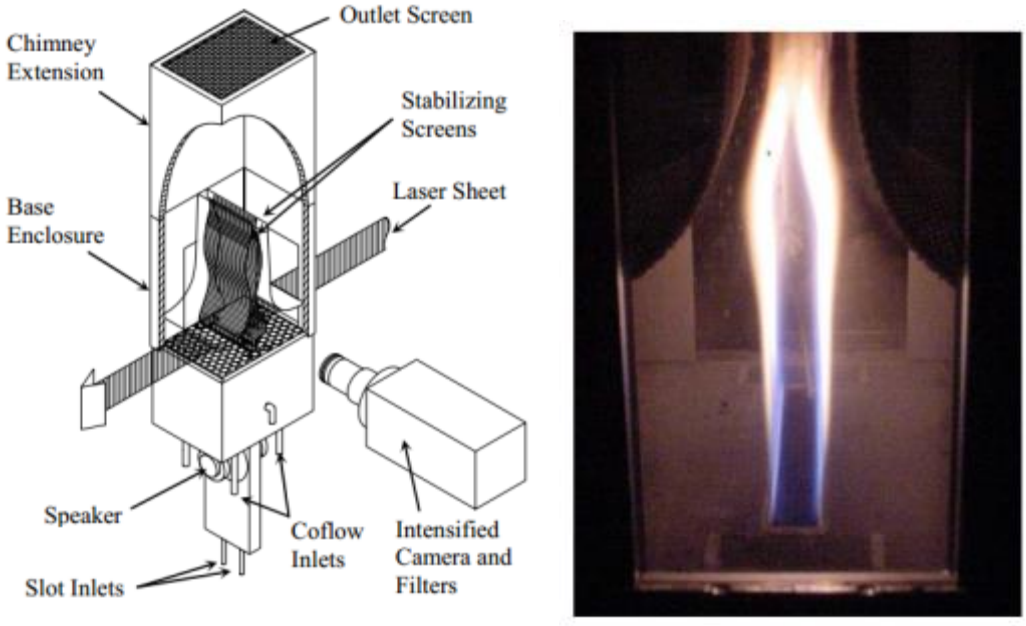

Figure 2.10 Shaddix's experimental set up for the inverse flame [15]

Sunderland et al. [16] used inverse spherical flames to distinguish the effects of convection direction and stoichiometry on soot formation. Figure 2.11 shows four different configuration of the test using a spherical porous burner in 2.2 s drop facility. The burner was placed in a pressured vessel with supported fuel delivery system. Figure a and b are normal flames. Figure c and d are inverse flames. For the stoichiometric mixture fraction Z_{st}=0.064, the flame is yellow and when Z_{st}=0.78 the flame is soot free regardless of the convection direction.

Soot particles were formed in the flame. In flame (a) the convection direction is toward the oxidizer where the soot growth is eliminated. In flame (c), which is an inverse flame, the convection direction is toward fuels side which enhanced the soot growth.

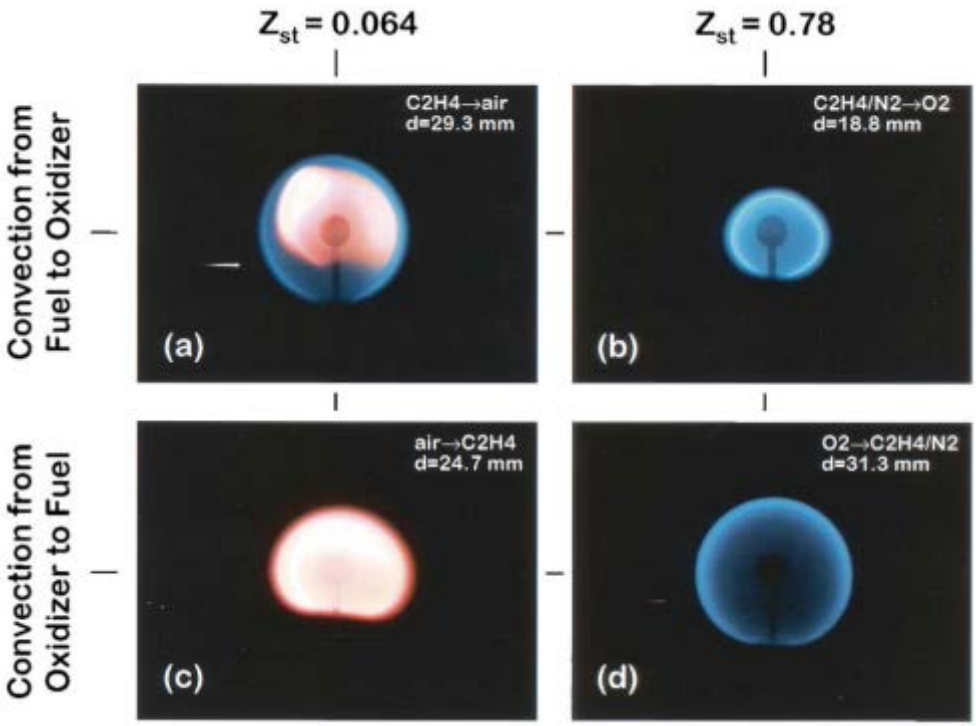

Figure 2.11 Color images of microgravity flames from the burner. (a) Ethylene issuing into air (b) diluted ethylene issuing into oxygen (c) air issuing into ethylene (d) oxygen issuing into diluted ethylene. [16]

Bhatia et al [17] presented a global chemistry calculation for inverse flames with oxygen enhancement [4] using an axisymmetric CFD code. The temperature contour they computed qualitatively matched the shape and location of the color changes observed in the photographs. They also showed the axial plot for gas velocity and temperature. The finding was that the inverse flame is less sensitive with respect to the oxygen and gravity variation compare to the normal diffusion flame.

Kaplan and Kailasanath [18] examined the effects of flow-field configuration on soot formation in inverse diffusion flames using direct numerical simulation. The result was comparable to the experimental results conducted by others. Table 1 summarized the main differences of soot formation in normal and inverse diffusion flames with

same fuel and air velocities. It shows that the inverse flames produce much less soot than the normal diffusion flames. The surface growth rate for inverse flames is also smaller because of the unfavorable temperature and stoichiometric conditions along the soot path. Inverse flame emits soot due to the fact that surface growth continues after oxidation ceases.

Table 1 Differences in sooting characteristics between normal and inverse diffusion flames [18]

	Normal 10/10	Inverse 10/10
Peak soot volume fraction	6.2e-7	3.6e-9
Peak soot number density (cm^{-3})	9.1e9	1.6e9
Total soot mass (g)	6.2e-7	9.6e-10
Peak mean particle diameter (nm)	59	21
Location of sooting region	Annular region, fuel-rich side of flame sheet	Fuel-rich region on top of flame sheet
Peak nucleation rate (g/cm^3-s)	3.5e-8	3.1e-8
Peak surface growth rate (g/cm^3-s)	1.9e-5	1.9e-7
Peak OH oxidation rate (g/cm^3-s)	3.5e-5	1.3e-8
Peak O_2 oxidation rate (g/cm^3-s)	1.9e-6	1.1e-7
Particle pathlines show that:	All soot formation and destruction processes begin before particle crosses flame sheet.	All soot formation and destruction processes begin after particle crosses flame sheet
	Peak soot volume fraction occurs before particle crosses stoichiometric surface.	Peak soot volume fraction maintained for long residence time due to very low oxidation rates.
	Creation and destruction processes cease around same time, resulting in no soot emission.	Surface growth continues after oxidation ceases, causing flame to emit soot.

2.3 Quenching limit

Cheng et al. [8] investigated the quenching flow velocity of methane microjet flames. The tube diameters range from 186 to 778 μm. Figure 2.12 shows the flames just above the quenching limit.

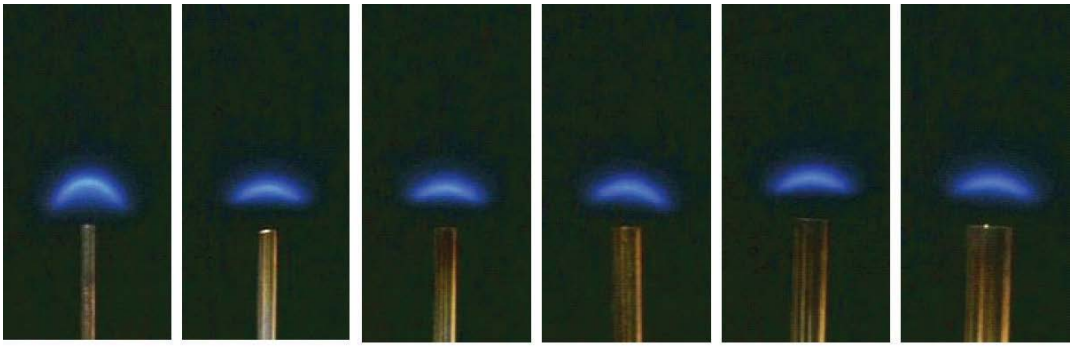

Figure 2.12 Methane flames close to the quenching limits. [8]

The flame shapes and the standoff distances are similar regardless of the tube diameter. When the flame is near the quenching limit, the spherical flame is dominated by diffusion and the buoyancy is less important at the moment. In addition, the flame length is hypothesized to be equal to the quenching distance. The author reviewed a series of correlations for jet diffusion lengths.

The model of Turns [19] that does not include the buoyancy:

$$L_f = \frac{3}{8\pi}\frac{Q_f}{DY_{F,stoic}} \tag{2.2}$$

where L_f is the flame length, Q_f is the volumetric flow rate, D is the mass diffusivity and $Y_{F,stoic}$ is the stoichiometric fuel mass fraction.

Roper's equation can be applied whether or not buoyancy is important:

$$L_f = \frac{Q_f}{4\pi D_O \ln(1+1/S)}\left(\frac{T_O}{T_f}\right)^{0.67} \tag{2.3}$$

where S is the molar stoichiometric oxidizer-fuel ratio, D_O is the mean diffusion coefficient, T_O is the oxidizer stream temperature where D_O is evaluated and T_f is the flame temperature.

Chung and Law [20] derived an equation that includes both axial streamwise effects and preferential diffusion:

$$[c(1+T_{O0})-Y_{O0}]+2(1+Y_{O0})\sum_{1}\sin(n\pi c)\exp[(Pe-\alpha_n)Z_f^*/2]/(n\pi)=0 \quad (2.4)$$

where c is the normalized half-width of the inner wall, Y_{O0} is the mass fraction of the oxidizer in the oxidizer stream, $\alpha_n=(Pe^2+4\pi^2n^2)^{1/2}$ and Z_f^* is the normalized flame height.

They analyzed the experimental results based on Roper's equation [12]. Roper's prediction agrees well with the experimental measurements as shown in Figure 2.13. It was also found that the result align with the straight line of $\mathrm{Re}\times d=$ const.

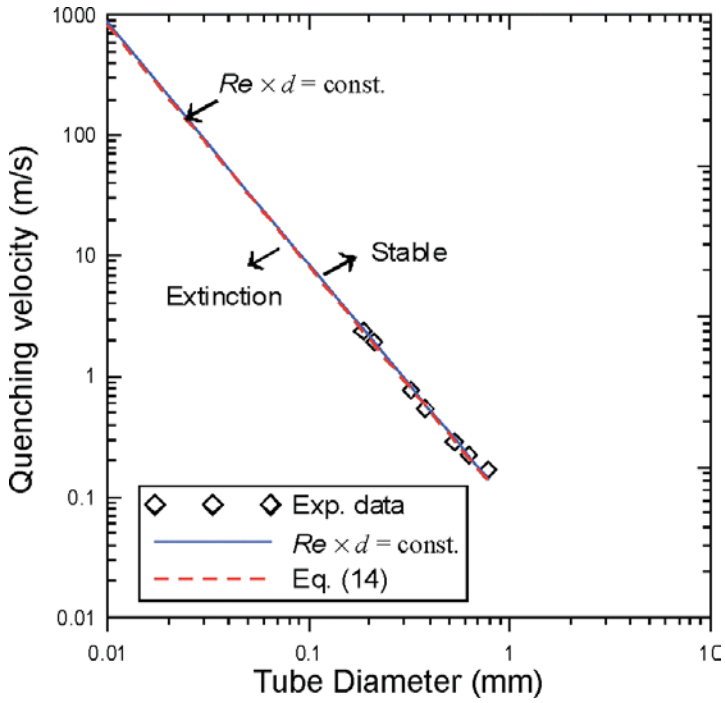

Figure 2.13 Methane quenching velocity as a function of tube diameter [8]

The nozzle configuration effect was also studied by conducting the numerical simulation for d=186, 324, 529 μm. A full set of governing equation and skeletal

chemical mechanisms were calculated. The comparison of these burner diameters with different wall thermal conductivities are shown in Figure 2.14.

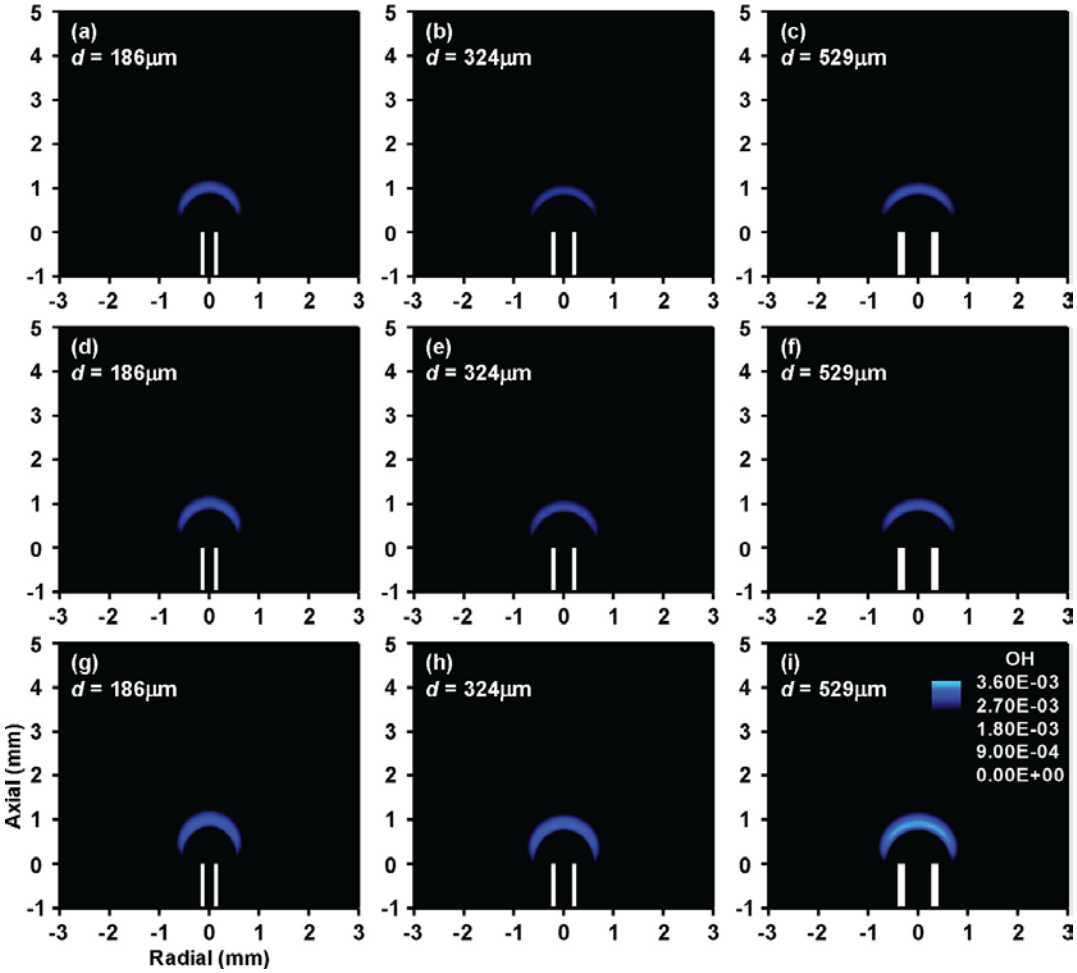

Figure 2.14 Computed OH mass fraction contour near the extinction limit [8]

The variation in quenching distance is within 5 % for the same diameter with different materials. However the gap between the bottom of the flame and the tube tip decreases for lower conductivity materials.

Butler et al [10] tested the hydrogen quenching limit on round-hole tube burners with different diameter, varying from 0.051 mm to 2.21 mm. Figure 2.15 shows their result

as well as results from other researchers. The quenching limit does not vary much with the diameter of the tube.

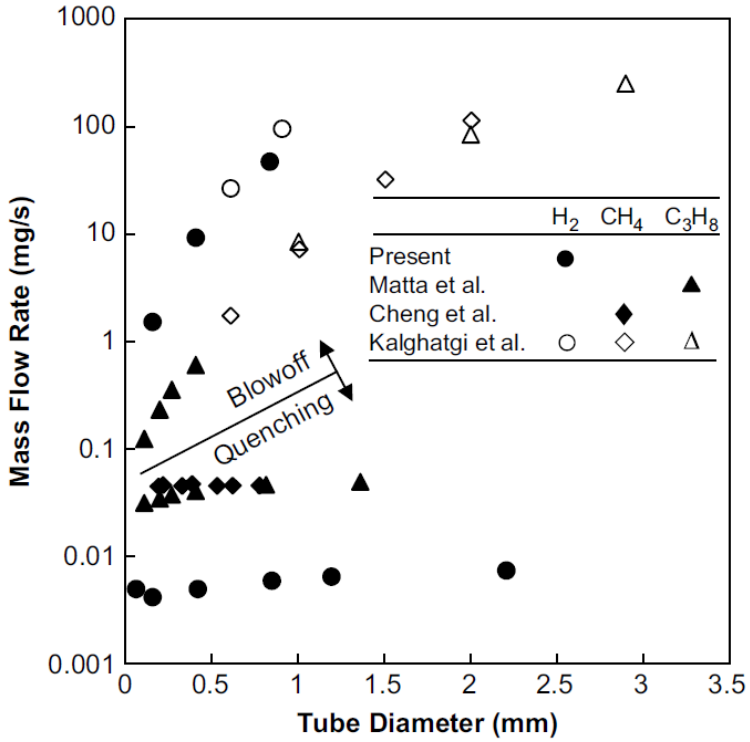

Figure 2.15 Mass flow rates at quenching and blow off limits with respect to tube diameter [10]

They also investigated the effect of burner configuration on the quenching limit of hydrogen. The difference occurred for smaller burner diameters due to the different heat loss effect. Figure 2.16 illustrates the three different burner configurations: pinhole, curved-wall and tube. The quenching mass flow rates for these three burners are shown in Figure 2.17. The pin-hole burner loses much of its heat to the ambient so it requires higher flow rates to maintain the flame. For the tube burner, the heat obtained by the tube largely goes back the fuel flow so the total energy in the system is not affected greatly. As for the curved-wall burner, the larger the curvature, the more the

heat is lost from the system. So the 6.4 mm curved-wall burner behaves like the pinhole burner while the 1.6 mm curved-wall burner behaves like the tube burner.

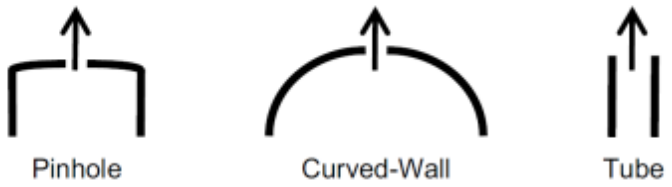

Figure 2.16 Different configurations of the round-hole burner [10]

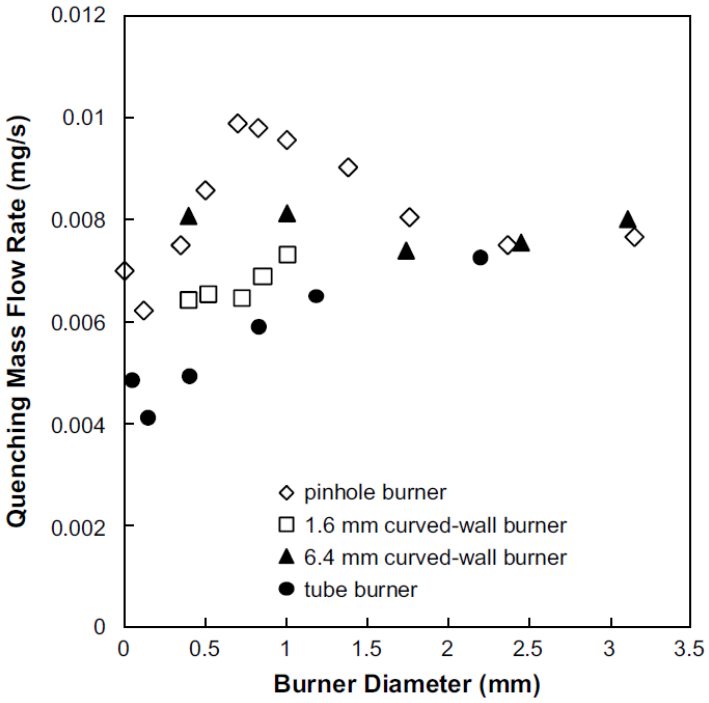

Figure 2.17 The quenching mass flow rates of different burner configurations [10]

Apart from the measurements of the quenching limits in the horizontal configuration, the tests were also conducted in vertical and inverted configurations. The result in the Figure 2.18 shows little effect of the orientations on the quenching limit.

This observation could also be proved by examining the Froude number, which in this case is about 0.17-0.39. It indicates that the flame is in the nonbuoyant region where the orientation has little effect on the burning behaviors.

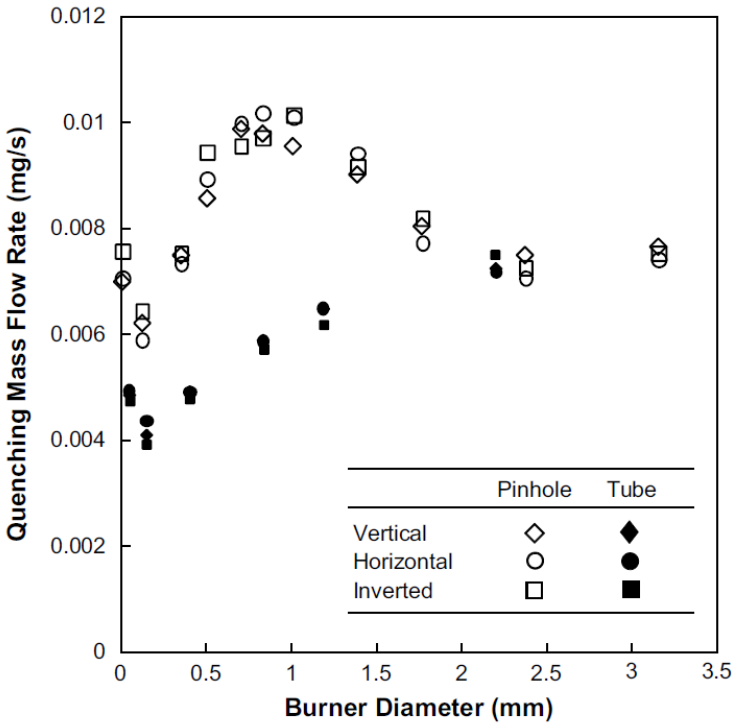

Figure 2.18 The quenching mass flow rates of different burner orientations [10]

Matta et al. [7] showed some results of quenching limits of propane on stainless steel hypodermic tubes with diameter ranging from 101 μm to 838 μm. The flame shape and the quenching distances were also found to be similar as presented in Figure 2.19.

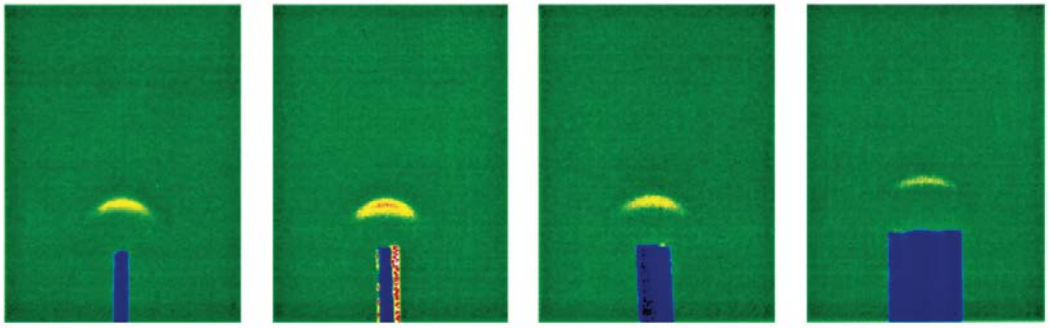

The quenching limit's dependency on the ambient air temperature was also studied. As shown in the Figure 2.20, the quenching flow rate of propane at three different sizes of tube diameter, 100, 178 and 254 μm, decreases as the ambient temperature increase to 500 °C. The reasoning for that could be the heat loss is eliminated by preheating the ambient. Similar effect goes with the premixed flame. The flammability of premixed gas decreases as its temperature increases.

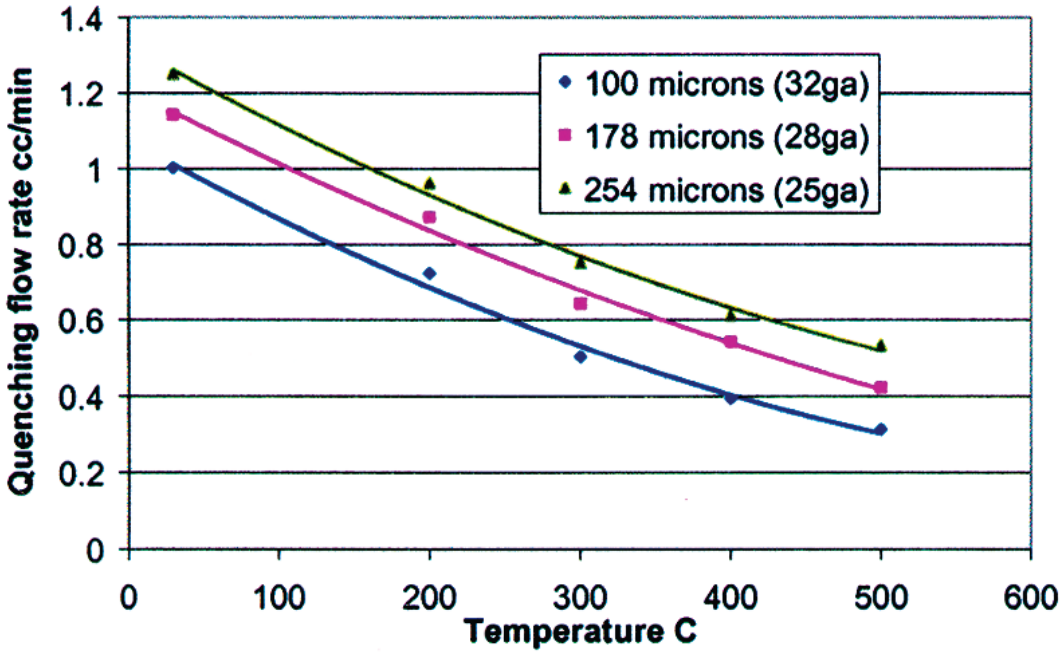

Figure 2.20 Quenching limit as a function of ambient temperature [7]

A region of premixed flame exists at the base part of a diffusion flame where the mixture of air and fuel happens as the fuel passes through the standoff distance. Figure 2.21 predicts the equivalence ratio along the radial axis at the quenching flow rate. It is generated by calculating the laminar flame equations. Compared to the blow-off limit, the combustible zone is much wider near the quenching limit leading to the hypothesis that it burns as premixed flame near the quenching limit.

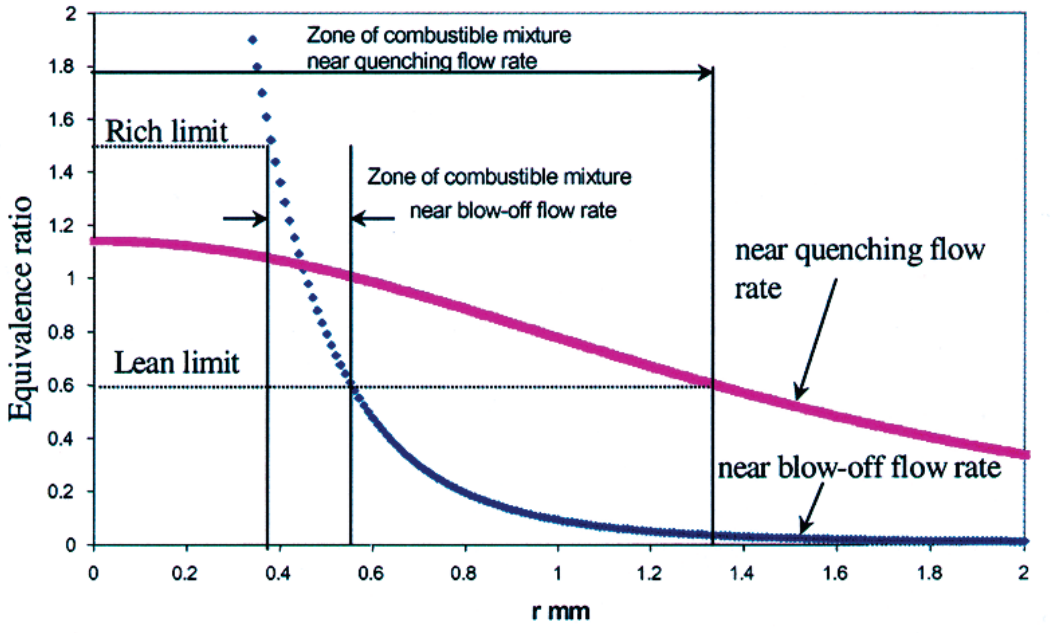

Figure 2.21 Equivalence ratio near quenching and blow-off with respect to radius [7]

However, in Cheng's paper [8], they presented the result of a careful numerical calculation, which generated the contour plot of velocities, temperature and species concentrations. The results are depicted in Figure 2.22. It strongly suggested that the flame burns as a diffusion flame near the quenching limit.

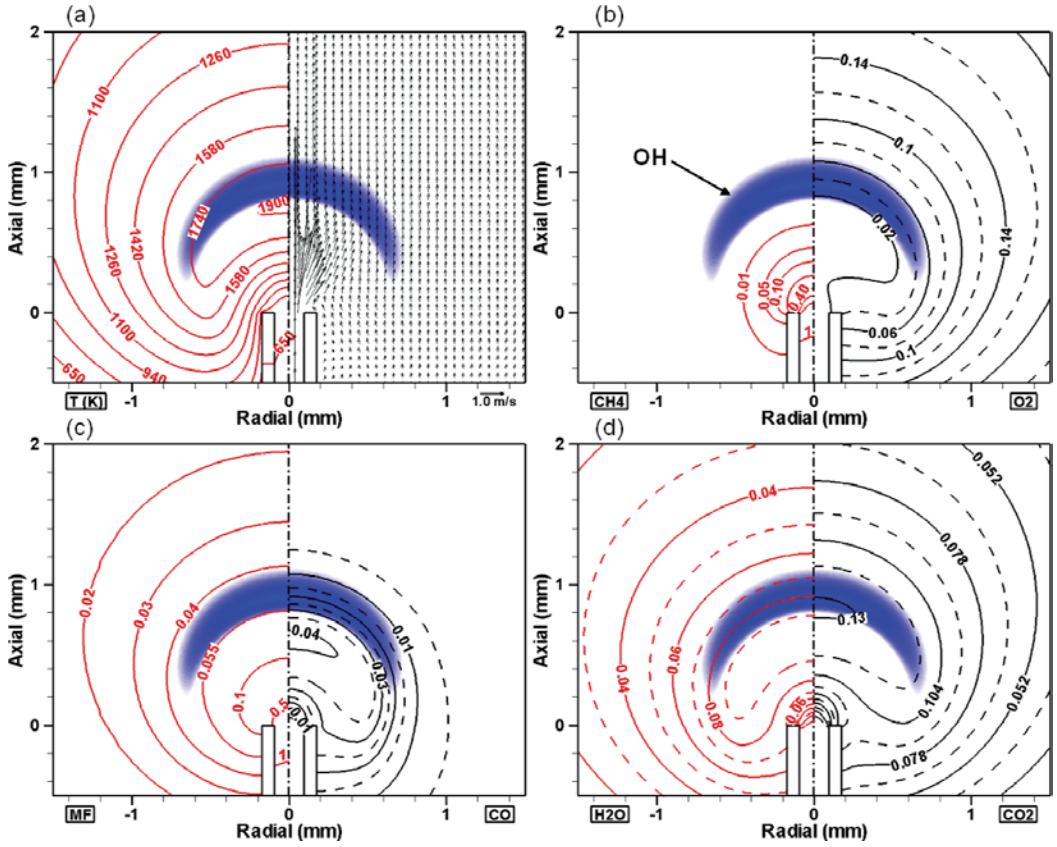

Figure 2.22 Numerical simulation of the flame close to the quenching limit [8]

3. Experimental

Brass co-flow burners were used in the experiment with central oxidizer ports of 0.75, 1.53, 3.02, 4.56 and 10.1 mm diameter and concentric fuel ports of 100 mm diameter. The fuel passage contains screens and 3.0 mm glass beads to provide a uniform fuel flow. A ceramic honeycomb section with 1.5 mm cell size is used as the final section of the fuel passage. A glass chimney was placed on top of the burner, covered with aluminum foil with a 13 mm diameter opening at the center (See Figure 3.1). The connections of these parts were sealed by O-rings.

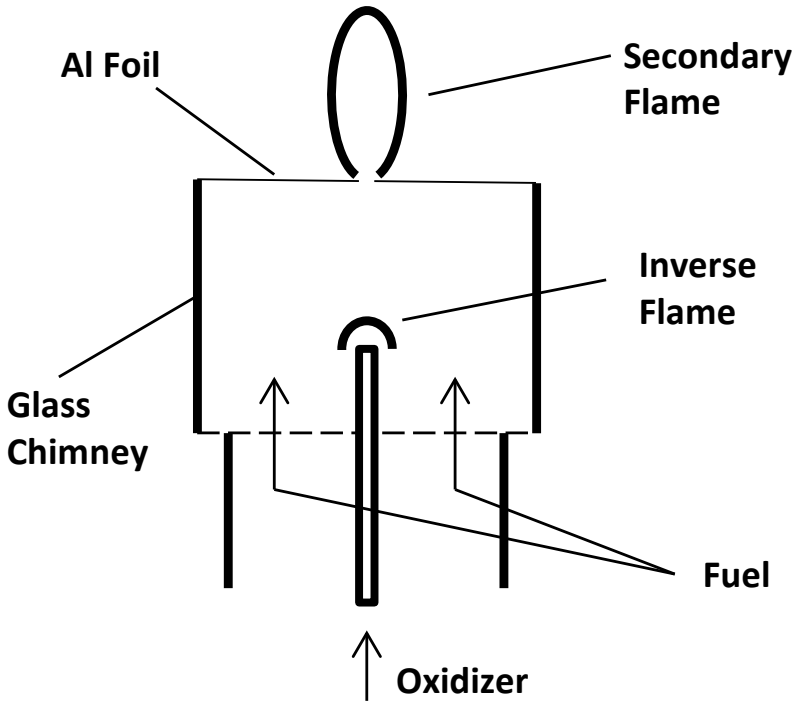

Figure 3.1 Schematic for the burner

The oxidizers used in the experiment were O_2 mixtures of 21%, 30%, 40% and 100% mole fraction in nitrogen mixed by partial pressure technique in a pressure vessel shown in Figure 3.2. The vessel was first filled with nitrogen and the resulting pressure

is recorded. Then the oxygen was filled until the pressure reaches a certain value that satisfies the required gas proportion based on the fact that partial pressure is proportional to the volume fraction under ideal gas law assumption.

Figure 3.2 Pressure vessel

The fuels were methane, ethylene and propane. Both fuel and oxidizer were delivered through a pressure regulator and an OMEGA® FL 5000 series rotameter as shown in Figure 3.3.

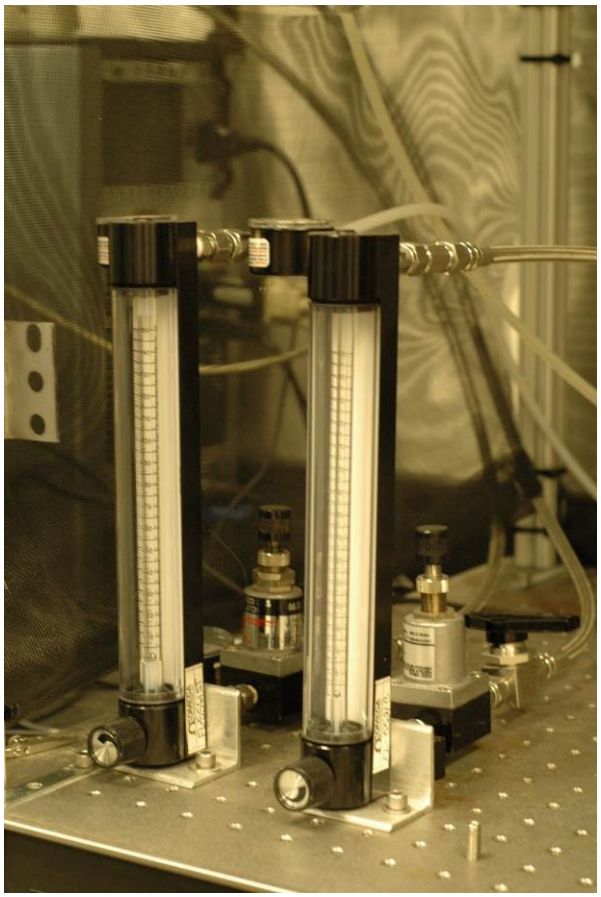

Figure 3.3 Flow system

All tests were conducted at normal lab pressure and temperature. The fuel flow rate was about 4 mg/s. Its ratio with the oxidizer flow rate was about 5- 10 times greater than the stoichiometric ratio. When the chimney was fully filled with fuel, the secondary flame was ignited. The inverse flame was then ignited at a relative high oxidizer flow rate by a platinum wire of 0.3 mm diameter placed close to the oxidizer port. The oxidizer flow rate was gradually decreased until the flame was quenched. The flow rate of oxidizer at quenching was recorded. Figure 3.4 shows the flame near the quenching limit. The ignition wire was moved to the side. Later these flow rates are calibrated by the glass soap bubble meter. The calibration result is shown in Figure 3.5.

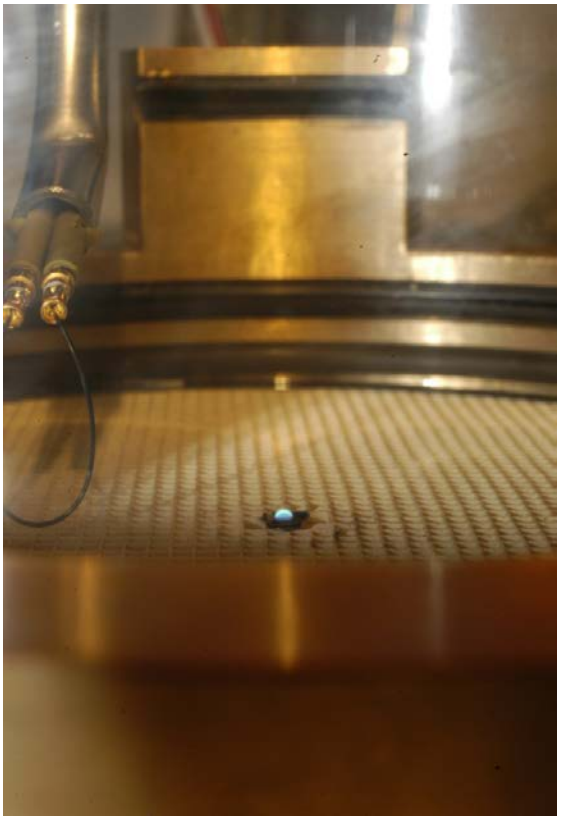

Figure 3.4 Colored photo of the experimental set up with the inverse flame at the center

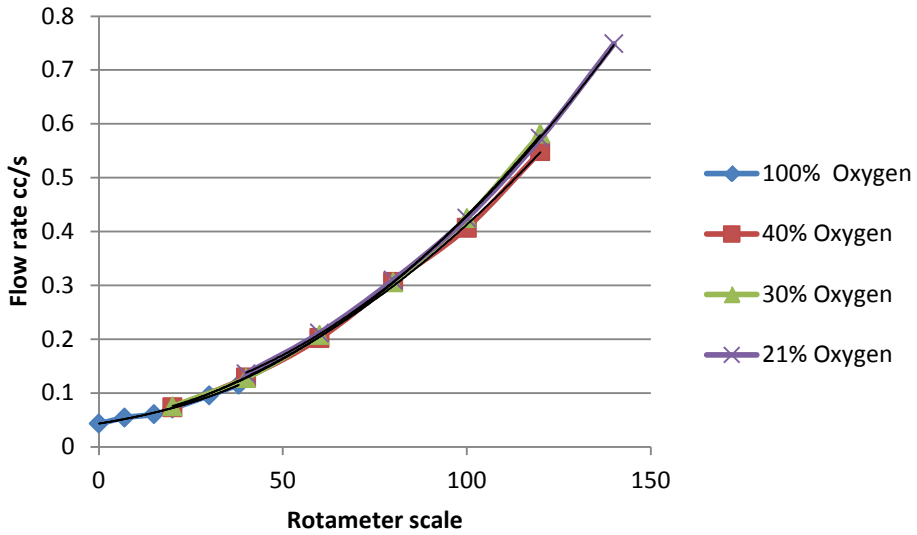

Figure 3.5 Calibration of the rotameter measurements

Butler [10] reported to use a K type thermocouple positioned above the port to detect the hydrogen flame quenching. In our case, the flames were sufficiently luminous that quenching could be observed visually. For large diameters, the flame was burning in the tube when it reached the quenching limit. In these cases, the flow rate of oxidizer was tuned up after the extinction to ensure the flame was indeed quenched.

The product of the combustion could be condensed on the glass chimney if the inverse flame burned long enough. Once this happened, the chimney was opened and cleaned to ensure a clear observation of the inverse flame.

Four to five tests were conducted for each condition to assure the repeatability. The estimated uncertainty in the reported quenching flow rates is $\pm 10\%$.

4. Results

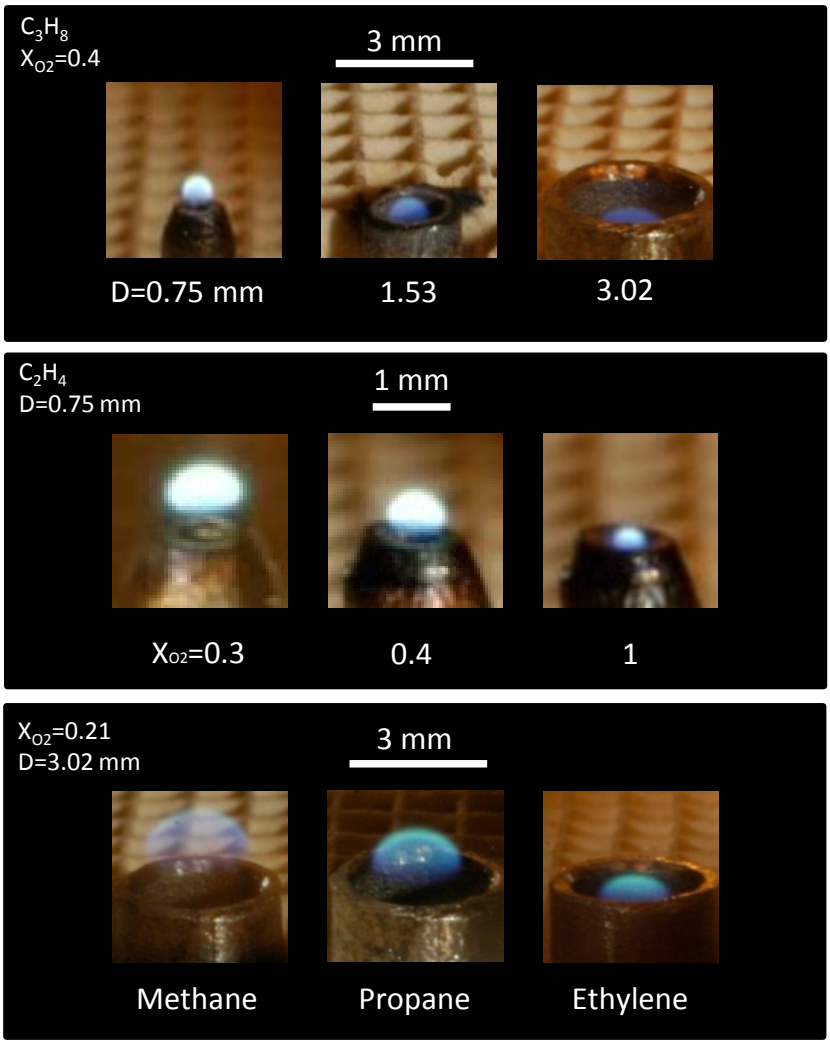

Figure 4.1 Color images of inverse flames close to their quenching limits.

Figure 4.1 shows images of three series of flames burning just above the quenching limits. The flame height, referring to the distance between the flame tip and the burner, varies with diameters, oxygen concentration and the fuel type. In the top series, the flame height decreases as the diameter of the port increases. For normal flame, however, the flame height is essentially independent of the burner tube diameter. As indicated in Figure 4.4, the series with different tube diameters have almost the same

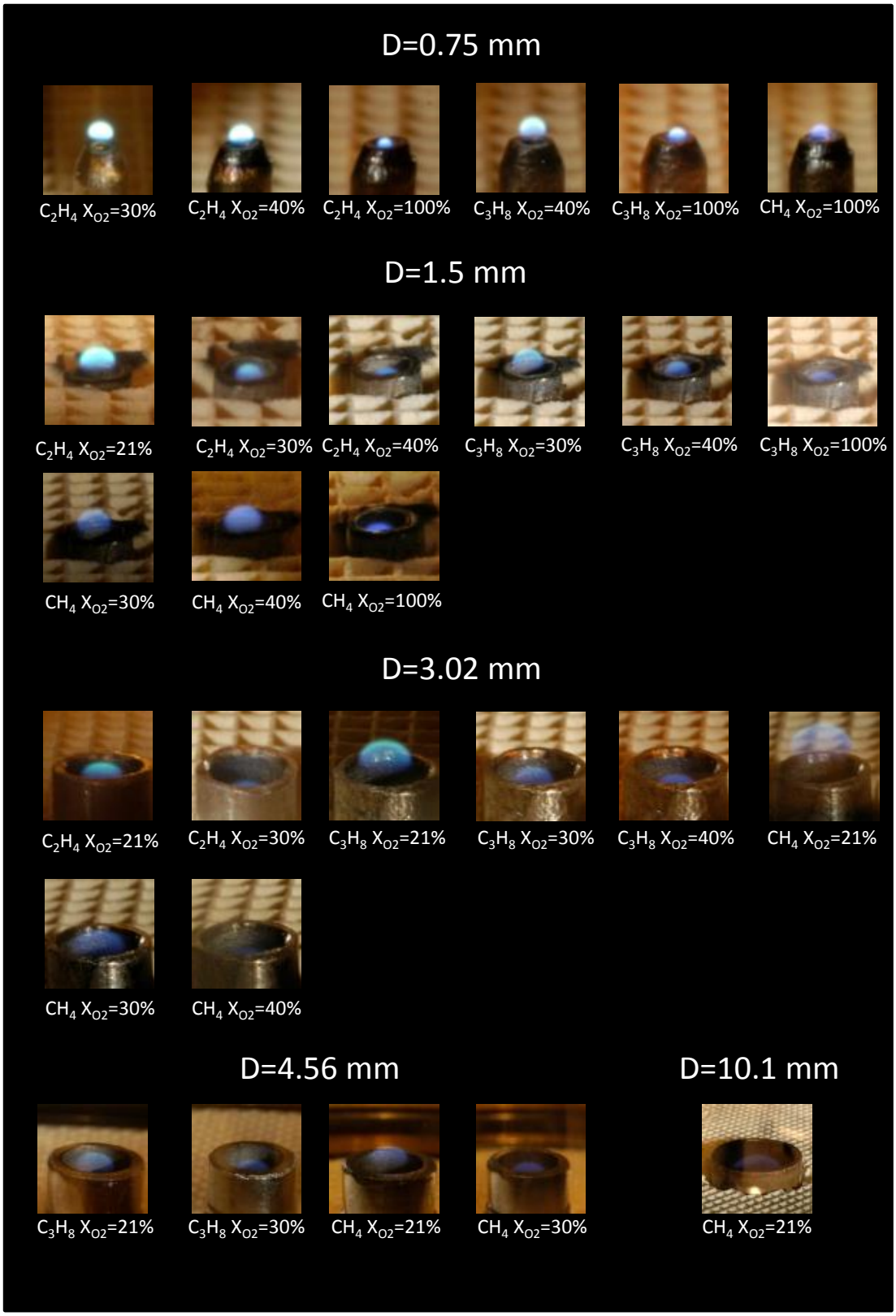

Figure 4.2 Color photos of the flame near quenching limits for all the tests

flow rate of oxidizer. Given the same mass flow rate, the larger the diameter of the port, the smaller the velocity would be. The same reasoning would also explain the two other

series (center and bottom in Figure 4.1). Since the diameters are the same, flow velocities correspond to mass flow rates and the flame height is reflected by the mass flow rate. A complete set of the test photos is shown in Figure 4.2.

Figure 4.3 shows the quenching limits for inverse flames burning in methane, ethylene and propane on different burners with respect to X_{O2}. The quenching limits generally decrease as X_{O2} increases. They fitted in a power function with an exponent of -1.4 to -1.6. The quenching limits for different fuels show a clear distinction among each other.

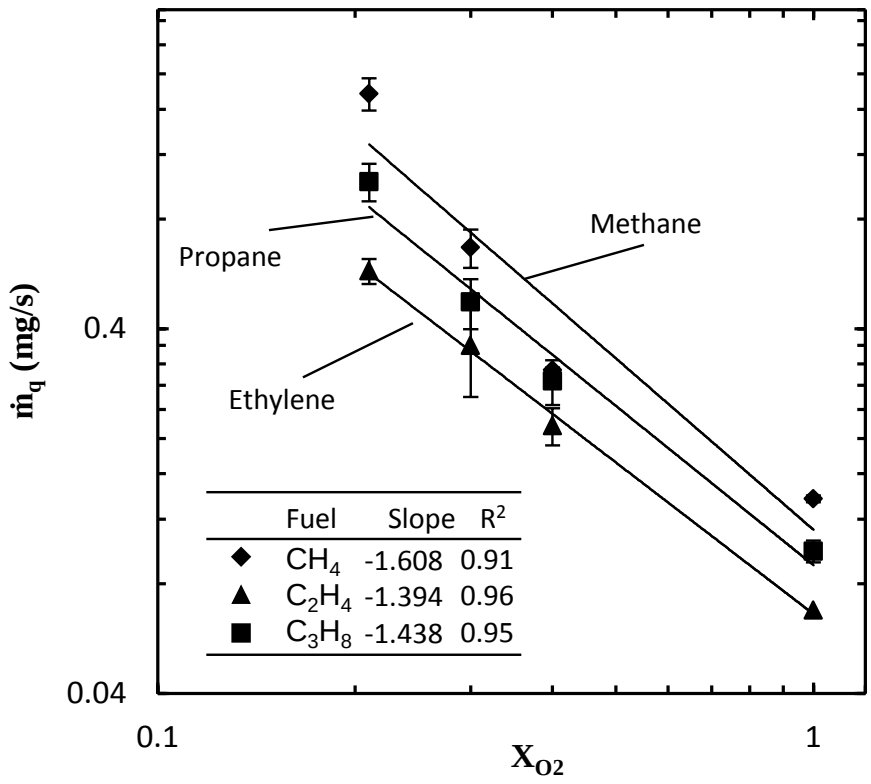

Figure 4.3 Quenching mass flow rate of oxidizers injecting into CH_4, C_2H_4 and C_3H_8 with respect to X_{O2}. The error bars include the results for different burner diameters.

Figure 4.4 depicts the quenching mass flow rate with respect to the burner diameter. The methane/air and propane/air inverse flame quenching limits by Yoshimoto et al

[21]. are also plotted. It shows that the mass flow rates at quenching of inverse flames do not vary largely with the burner diameter. That is consistent with the quenching limits' dependency on burner diameters for the normal flames reported in Butler [10] for methane and propane. The line fits represent the mean values for each fuel. The mass flow rates were multiplied by $X_{O2}^{-1.5}$ to reduce the oxidizer effect.

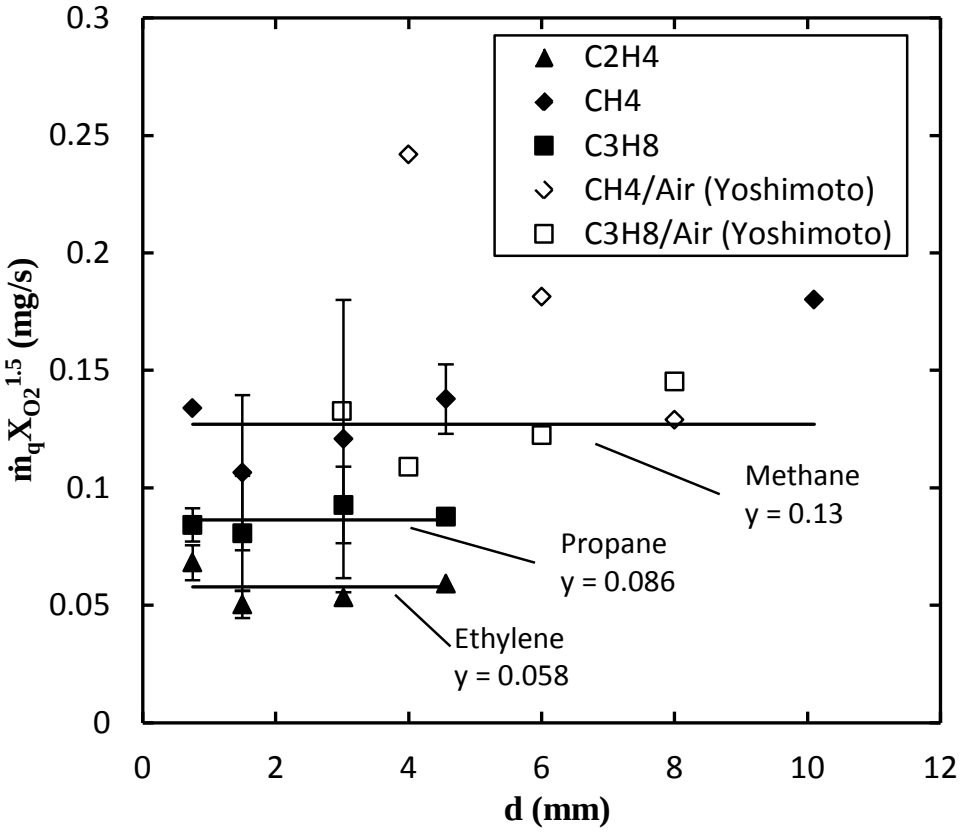

Figure 4.4 Quenching mass flow rate of oxidizers with respect to burner diameters. The error bars include the results for different oxygen concentrations.

Figure 4.5 shows that the quenching limits are proportional to the quenching distances of the corresponding fuels (see Table 2). The mass flow rates are again multiplied by $X_{O2}^{-1.5}$. In average, the quenching limits for methane are greater than that for propane and the quenching limits for propane are greater than that for ethylene.

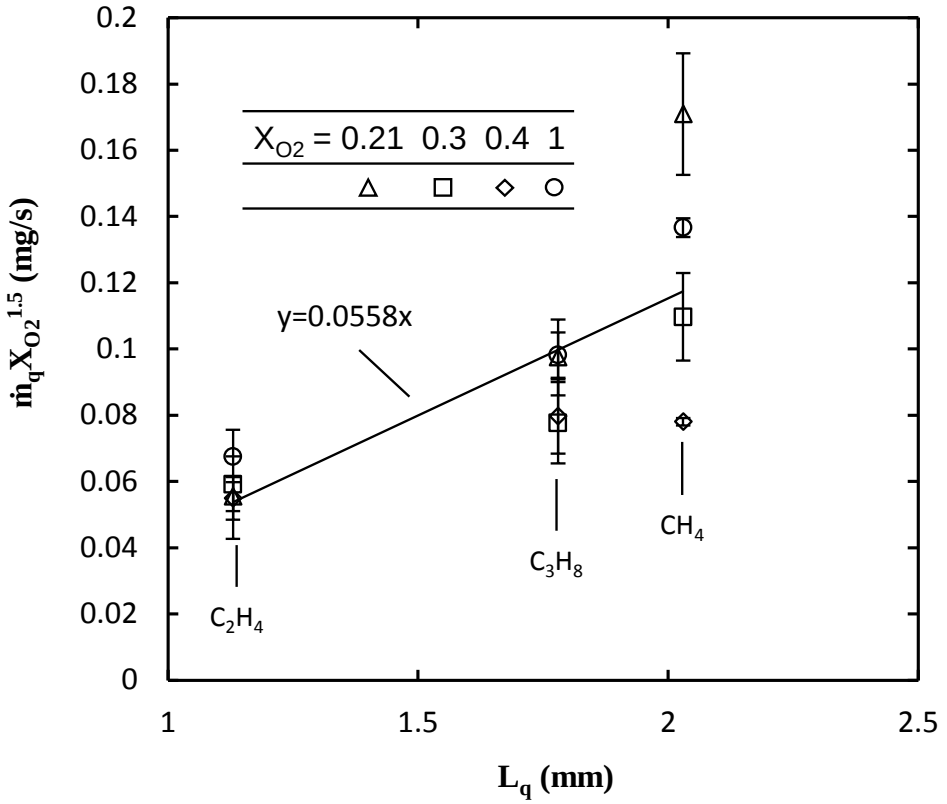

Figure 4.5 Quenching mass flow rate of oxidizers with respect to quenching distances. The error bars include the results for different burner diameters.

Matta [7] and Cheng [8] reported the quenching heat release rates for methane and propane were about 3 and 2.78 W. In our study, the heat release rates for inverse flames at quenching were in the range from 1- 2 W. The result is shown in Figure 4.6.

The heat release rates presented here are calculated by

$$HRR_q = \dot{m}_q'' X_{O2} r \Delta h_c \tag{4.1}$$

where r is the stoichiometric fuel to oxygen mass fraction. Since the combustion occurs at its quenching limit is close to ideal complete combustion, Δh_c used here is taken as the thermodynamic value shown in Table 2.

Table 2 Selected properties of methane, ethylene and propane

Fuel	L_q (mm)	S_L (cm/s)	μ (g/m-s)	Δh_c(kJ/g)
CH_4	2.03	37.3	1.09E-2	50.1
C_2H_4	1.13	58.2	1.00E-2	47.1
C_3H_8	1.78	42.9	7.95E-3	46

Values L_q and S_L for methane and propane are from [22], L_q for ethylene is from [23], S_L for ethylene is from [24], μ is from [25] and Δh_c is from [26].

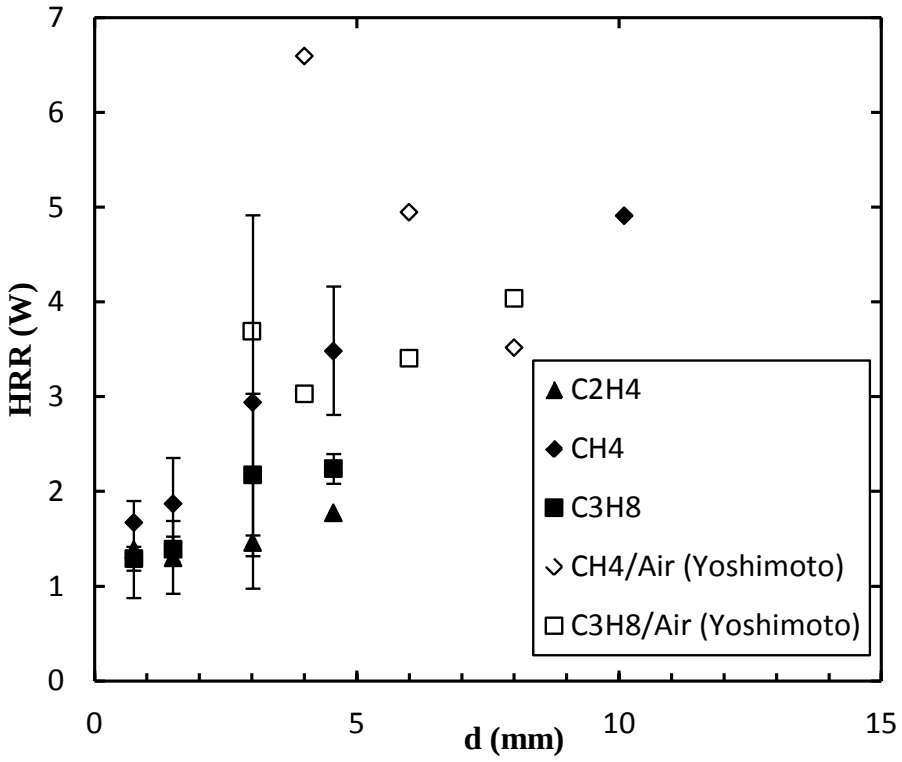

Figure 4.6 Heat release rate at the quenching limit with respect to burner diameter. The error bars include the results for different oxygen concentrations.

Ignition is difficult for smaller nozzle diameters. For ethylene in the air, the inverse flame could not be ignited for 0.75 mm diameter nozzle. For methane, the inverse flame never got ignited on 0.75 mm oxidizer port except for 100% oxygen. For propane, no results were gained for 0.75 mm diameter for 21% and 30% oxygen. The detailed quenching limit results are listed in Table 3.

Table 3 Quenching limit measurements for all tests

Quenching limit (mg/s) of oxidizers in ethylene				
D (mm)\X_{O2}	0.21	0.3	0.4	1
0.75		0.46	0.24	0.068
1.5	0.58	0.28	0.19	
3.02	0.53	0.33		
4.56	0.61			

Quenching limit (mg/s) of oxidizers in methane				
D (mm)\X_{O2}	0.21	0.3	0.4	1
0.75				0.13
1.5		0.63	0.30	0.14
3.02	1.87	0.63	0.31	
4.56	1.58	0.75		
10.1	1.87			

Quenching limit (mg/s) of oxidizers in propane				
D (mm)\X_{O2}	0.21	0.3	0.4	1
0.75			0.28	0.09
1.5		0.40	0.26	0.11
3.02	1.13	0.48	0.33	
4.56	0.90	0.54		

5. Conclusions

The quenching limits of inverse diffusion flames have been measured for different fuel-oxidizer combustion on different sizes of burners. The fuels considered were methane, ethylene and propane. The O_2 mole fractions were 0.21, 0.3, 0.4 and 1. The diameters of the oxidizer port were 0.75, 1.53, 3.02, 4.56 and 10.1 mm. The key findings are:

1. The quenching limits of inverse flames decreases as the oxygen concentration increases. Based on our analysis, it scales with $X_{O2}^{-1.5}$.
2. The quenching limits of inverse flames do not depend largely on the diameter of the oxidizer port. This conclusion is the same for the normal diffusion flame as for its quenching limits' dependency on the burner diameter.
3. The quenching limits of inverse flames are proportional to the fuel quenching distance.
4. The heat release rates of the quenching inverse flames vary from 1 – 2 W. They are lower than the heat release rates of normal diffusion flames with the same configurations.

References

1. B. E. Williams, "The Effects of Oxygen-Enriched air on Firefighter Job Performance," (1998).
2. J. M. Butler, "A Computational Model of Dissipation of Oxygen from an Outward Leak of a Closed-Circuit Breathing Device," (2007).
3. M. Alan, "The inverse flame," Physics Education **42**, 434 (2007).
4. P. B. Sunderland, S. S. Krishnan, and J. P. Gore, "Effects of oxygen enhancement and gravity on normal and inverse laminar jet diffusion flames," Combustion and Flame **136**, 254-256 (2004).
5. M. A. Mikofski, T. C. Williams, C. R. Shaddix, and L. G. Blevins, "Flame height measurement of laminar inverse diffusion flames," Combustion and Flame **146**, 63-72 (2006).
6. A. Sobiesiak, and J. C. Wenzell, "Characteristics and structure of inverse flames of natural gas," Proceedings of the Combustion Institute **30**, 743-749 (2005).
7. L. M. Matta, Y. Neumeier, B. Lemon, and B. T. Zinn, "Characteristics of microscale diffusion flames," Proceedings of the Combustion Institute **29**, 933-939 (2002).
8. T. S. Cheng, C. P. Chen, C. S. Chen, Y. H. Li, C. Y. Wu, and Y. C. Chao, "Characteristics of microjet methane diffusion flames," Combustion Theory and Modelling **10**, 861-881 (2006).
9. J. Baker, M. E. Calvert, and D. W. Murphy, "Structure and Dynamics of Laminar Jet Micro-Slot Diffusion Flames," Journal of Heat Transfer **124**, 783-790 (2002).
10. M. S. Butler, C. W. Moran, P. B. Sunderland, and R. L. Axelbaum, "Limits for hydrogen leaks that can support stable flames," International Journal of Hydrogen Energy **34**, 5174-5182 (2009).
11. H. D. Ross, *Microgravity combustion fire in free fall* (Academic Press, 2001).
12. F. G. Roper, "The prediction of laminar jet diffusion flame sizes: Part I. Theoretical model," Combustion and Flame **29**, 219-226 (1977).
13. M. A. Mikofski, T. C. Williams, C. R. Shaddix, A. C. Fernandez-Pello, and L. G. Blevins, "Structure of laminar sooting inverse diffusion flames," Combustion and Flame **149**, 463-478 (2007).
14. C. R. Shaddix, T. C. Williams, L. G. Blevins, and R. W. Schefer, "Flame structure of steady and pulsed sooting inverse jet diffusion flames," Proceedings of the Combustion Institute **30**, 1501-1508 (2005).
15. L. G. Blevins, R. A. Fletcher, B. A. Benner Jr, E. B. Steel, and G. W. Mulholland, "The existence of young soot in the exhaust of inverse diffusion flames," Proceedings of the Combustion Institute **29**, 2325-2333 (2002).
16. P. B. Sunderland, R. L. Axelbaum, D. L. Urban, B. H. Chao, and S. Liu, "Effects of structure and hydrodynamics on the sooting behavior of spherical microgravity diffusion flames," Combustion and Flame **132**, 25-33 (2003).
17. P. Bhatia, V. R. Katta, S. S. Krishnan, Y. Zheng, P. B. Sunderland, and J. P. Gore, "Simulations of normal and inverse laminar diffusion flames under oxygen

enhancement and gravity variation," Combustion Theory and Modelling **16**, 774-798 (2012).
18. C. R. Kaplan, and K. Kailasanath, "Flow-field effects on soot formation in normal and inverse methane–air diffusion flames," Combustion and Flame **124**, 275-294 (2001).
19. S. R. Turns, *An introduction to combustion : concepts and applications* (WCB/McGraw-Hill, 2000).
20. S. H. Chung, and C. K. Law, "Burke–Schumann Flame with Streamwise and Preferential Diffusion," Combustion Science and Technology **37**, 21-46 (1984).
21. T. Yoshimoto, Y. Kato, N. Kubo, D. Ito, and K. Takagi, "Stability Limits and Behaviors of the Inverse Diffusion Flame," 5th Asia-Pacific Conference on Combustion (2005).
22. A. M. Kanury, *Introduction to combustion phenomena : (for fire, incineration, pollution, and energy applications)* (Gordon and Breach, 1975).
23. I. Glassman, *Combustion* (Academic Press, 1996).
24. A. Gutkowski, "Laminar Burning Velocity under Quenching Conditions for Propane-Air and Ethylene-Air Flames," Archivum Combustionis **26**, 163-173 (2006).
25. R. C. Weast, and M. J. Astle, *CRC Handbook of chemistry and physics* (CRC Press Inc. , 1979).
26. J. G. Quintiere, *Fundamentals of fire phenomena* (John Wiley, 2006).